


ORIGINAL ARTICLE

Thermal properties of 2:1 bismuth borate: Temperature-dependent characterizations of lone electron pairs

M. Mangir Murshed^{1,2}  | Hilke Petersen^{1,2} | Michael Fischer^{2,3} | Mariano Curti^{4,5} | Cecilia B. Mendive^{4,5} | Volodymyr Baran⁶ | Anatoliy Senyshyn⁶ | Thorsten M. Gesing^{1,2}

¹Institute of Inorganic Chemistry and Crystallography, University of Bremen, Bremen, Germany

²MAPEX Center for Materials and Processes, University of Bremen, Bremen, Germany

³Crystallography/Geosciences, University of Bremen, Bremen, Germany

⁴Departamento de Química, Facultad de Ciencias Exactas y Naturales, Universidad Nacional de Mar del Plata, Mar del Plata, Argentina

⁵Instituto de Investigaciones Físicas de Mar del Plata, CONICET/Facultad de Ciencias Exactas y Naturales, Universidad Nacional de Mar del Plata, Mar del Plata, Argentina

⁶Research Neutron Source Heinz Maier-Leibnitz (FRM II), Technische Universität München, Garching, Germany

Correspondence

M. Mangir Murshed, Solid State Chemical Crystallography, Institute of Inorganic Chemistry and Crystallography, University of Bremen, Bremen, Germany.
Email: murshed@uni-bremen.de

Abstract

Applications of bismuth borate ceramics require understanding of the microscopic features, leading to macroscopic behaviors such as thermal expansion. We report the structural and spectroscopic features of $\text{Bi}_4\text{B}_2\text{O}_9$ between 4 K and 900 K using a combination of temperature-dependent neutron and X-ray powder diffractions and Raman spectroscopy. Lattice thermal expansion was modeled using the Debye-Einstein-Anharmonicity (DEA) fit. The model also follows four independent thermal expansion tensors of the monoclinic system. Phonon density of states obtained from the density functional theory (DFT) calculations helps to understand the low Debye temperature calculated from the metric expansion as well as from the isotropic atomic displacement parameters. Both Wang-Liebaw eccentricity (WLE) parameter and Liebaw density vector (LDV) are calculated from the structural data and from the DFT calculation, respectively. Whereas, the dimensionless absolute value of WLE measures the degree of deformation of the electronic deformation density of the $6s^2$ lone electron pairs (LEPs) of the Bi^{3+} cations, LDV additionally shows the changes of the orientation of the LEP-lobes as function of temperature. Analyses of the temperature-dependent frequencies of some selected Raman modes support the choice of the elastic model of the Debye approach.

1 | INTRODUCTION

Bismuth borates ($x\text{Bi}_2\text{O}_3 \cdot y\text{B}_2\text{O}_3$) have been an intense interest since the discovery of promising nonlinear optical properties in BiB_3O_6 .¹ High double-refraction was reported for $\text{Bi}_4\text{B}_2\text{O}_9$.² $\text{Bi}_3\text{B}_5\text{O}_{12}$ showed stimulated Raman scattering³ and luminescence properties.⁴ Levin and McDaniel reported the binary phase diagram of Bi_2O_3 - B_2O_3 , giving five bismuth borates with different $x:y$ ratios: $\text{Bi}_{24}\text{B}_2\text{O}_{39}$ (Bi:B = 12:1), $\text{Bi}_4\text{B}_2\text{O}_9$ (Bi:B = 2:1), $\text{Bi}_3\text{B}_5\text{O}_{12}$ (Bi:B = 3:5), BiB_3O_6 (Bi:B = 1:3) and $\text{Bi}_2\text{B}_8\text{O}_{15}$ (Bi:B = 1:4).⁵

Much later, metastable BiBO_3 (Bi:B = 1:1),⁶ and $\text{Bi}_{24.5}\text{BO}_{38.25}$ (Bi:B ~ 25:39)⁷ were added to the series. A number of correlations were proposed between the x/y ratio and, (a) the number of BO_3 triangles and BO_4 tetrahedra in borate groups, (b) the average coordination number of Bi atoms, (c) and the degree of distortion of the Bi polyhedra.⁸ The role of Bi^{3+} $6s^2$ lone electron pairs (LEP) was suggested for the manifestation of the crystal physical features. The melting point and band gap energy seem also to be a function of x/y ratio as shown in Figure 1; both of which are found to be correlated to the magnitude of the

stereochemical activity of the LEPs which can be calculated from the Wang-Liebau eccentricity (WLE) parameter.^{15–17} In bismuth borates, the absorption bands depend on either the mutual interaction between the Bi^{3+} cations or the electron-lattice interaction due to the asymmetrically coordination of the bismuth polyhedra, in other words, the magnitude of WLE of the $\text{Bi}^{3+} 6s^2$ LEPs.⁴ In the present study we focus on understanding the temperature-dependent behavior of LEPs of $\text{Bi}_4\text{B}_2\text{O}_9$, leading to macroscopic thermal expansion.

The crystal structure of $\text{Bi}_4\text{B}_2\text{O}_9$ is shown in Figure 2.¹⁸ Stacks of planar BO_3 groups are rotated with respect to each other, can be seen along the **b**-direction. The BO_3 triangles are isolated with B(1)-B(2) minimum distance of about 318 pm, which is an uncommon feature in metal borates. Thus, the structure does not contain borate polymers. Each bismuth polyhedron connects the BO_3 groups forming the three-dimensional network. The Bi–O distances are highly spread within different coordination numbers (Figure 2). The Bi(1), Bi(2), Bi(3) and Bi(4) atoms are, respectively, six-, seven-, seven- and eightfold coordinated within a cut-off distance of 300 pm.

Thermal behaviors ultimately determine the applicability of a material whether to exploit its physical properties. As such, thermal expansion data are prerequisites for applications of materials at any given temperature for both microscopic and macroscopic matching conditions. It is unambiguously conceived that applications of bismuth borates require knowledge of thermal expansion

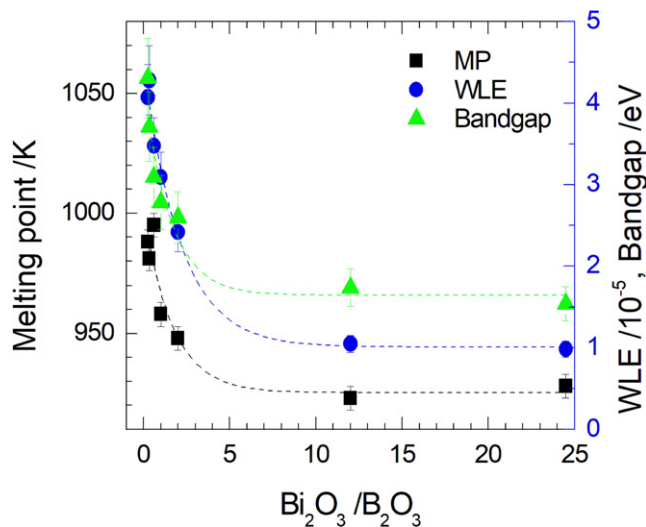


FIGURE 1 Correlation between the $\text{Bi}_2\text{O}_3/\text{B}_2\text{O}_3$ ratio and the melting point (MP), absolute value of Wang-Liebau eccentricity (WLE) parameter and electronic bandgap. The WLE parameter are calculated from the crystal data of $\text{Bi}_2\text{B}_8\text{O}_{15}$,⁹ BiB_3O_6 ,¹⁰ $\text{Bi}_3\text{B}_5\text{O}_{12}$,¹¹ BiBO_3 ,⁶ $\text{Bi}_4\text{B}_2\text{O}_9$,¹² $\text{Bi}_{24}\text{B}_2\text{O}_{39}$,¹³ $\text{Bi}_{24.5}\text{BO}_{38.25}$.⁷ The corresponding bandgaps are taken from ref. 14 and plotted along with 10% uncertainty of the respective value

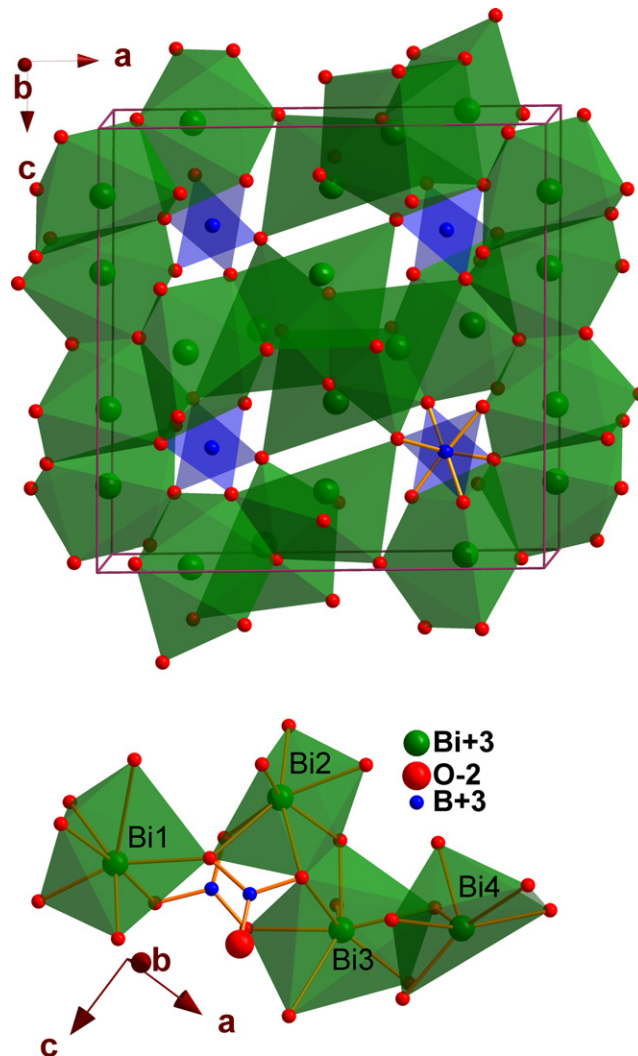


FIGURE 2 Crystal structure of $\text{Bi}_4\text{B}_2\text{O}_9$, showing the BiO_x and BO_3 polyhedra and their connectivity

coefficients for optical, mechanical and electronic properties.⁴ However, to understand the microscopic features leading to macroscopic thermal expansion of bismuth borates is not straightforward as borates mostly show highly anisotropic thermal expansion even with negative tensor elements. For instance, the maximum negative thermal expansion in BiB_2O_6 was observed parallel to the zig-zag chain formed by the BO_3 and BO_4 polyhedra, while the maximum positive thermal expansion occurs parallel to the sheets where the $\text{Bi}^{3+} 6s^2$ lone electron pairs (LEPs) are oriented.¹⁹ The LEP provides a kind of flexibility to the bismuth coordination, which was assumed to be the origin of the positive maximum of the thermal expansion in BiB_2O_6 . The thermal behavior of bismuth borates mainly stems from their unique B–O bonding strength within the BO_x polyhedral unit. It is stated that BO_x groups keep their configurations even in melts and glasses.²⁰ Upon heating BO_x groups in a polymeric topology rotate to each other as

a 'hinge'.²¹ Filatov et al¹² reported the thermal expansion of $\text{Bi}_4\text{B}_2\text{O}_9$, which is, however, limited to above the room temperature, and a linear fit cannot predict the low temperature behavior. In a recent report, Schreuer et al²² demonstrated the thermoelastic properties of $\text{Bi}_4\text{B}_2\text{O}_9$, which is again limited to above the ambient condition. This report will particularly focus on the thermal expansion of $\text{Bi}_4\text{B}_2\text{O}_9$ for a wide temperature range between 4 K and 900 K followed by microscopic modeling, using temperature-dependent neutron and X-ray powder diffractions, and Raman spectroscopy.

2 | EXPERIMENTAL

2.1 | Synthesis

The $\text{Bi}_4^{11}\text{B}_2\text{O}_9$ powder sample was synthesized, using a stoichiometric mixture of $\text{Bi}(\text{NO}_3)_3 \cdot 9\text{H}_2\text{O}$ and $^{11}\text{B}(\text{OH})_3$ with additional 7.5 wt% of the latter phase in a platinum crucible heated at 973 K for 72 hours.

2.2 | Neutron powder diffraction

Temperature-dependent neutron powder diffraction (NPD) experiments were carried out between 4 K and 320 K with a temperature slice of 10 K on the high-resolution powder diffractometer SPODI at FRM-II, Germany.²³ A collimated beam of thermal neutrons ($\lambda = 154.812(2)$ pm) has been obtained at a take-off angle of 155° using the (551) reflection of a vertically focusing composite germanium monochromator. Data were collected in the 2θ range between 1° and 152° with a step size of 0.05° . Rietveld refinements were performed using the GSAS²⁴ platform with EXPGUI²⁵ interface. During the refinement, the scale factor, absorption coefficient and two profile shape parameters, lattice parameters, fractional coordinates of the atoms and their displacement parameters were optimized.

2.3 | X-ray powder diffraction

High-temperature X-ray powder diffraction (XRPD) measurements were carried out followed by Rietveld refinements with the fundamental parameter approach using the "Diffrac^{Plus} Topas 4.2" (Bruker AXS GmbH, Karlsruhe, Germany) software. Data were collected on a Bragg-Brentano PANalytical X'Pert MPD PRO diffraction system (PANalytical GmbH, Almelo, The Netherlands) equipped with a secondary Ni filter, $\text{CuK}\alpha$ radiation and an X'Celerator multi-strip detector using an HTK 1200N heating chamber (Anton Paar, Graz, Austria). The sample was prepared in a flat corundum sample holder, using acetone to submerge the powder sample and to produce small evaporation channels which served as an additional space for the

thermal expansion of the compound. Measurements were carried out between 300 K and 900 K in steps of 10 K. Each pattern was recorded from 10° to $130^\circ 2\theta$ with a step size of 0.0167° and a 90 s/step total data collection time. For the Rietveld refinement, the starting atomic coordinates were taken from the room-temperature neutron data. The low-temperature NPD (10 K-300 K) and the high-temperature XRPD (300 K-900 K) were used to study the lattice thermal expansion.

2.4 | Raman spectroscopy

Raman spectra were recorded on a LabRam ARAMIS (HORIBA Jobin Yvon GmbH Raman Spektroskopie, Bensheim, Germany) Micro-Raman spectrometer equipped with a laser working at 785 nm and less than 20 mW. Data were collected in the range 50 cm^{-1} to 1500 cm^{-1} with a spectral resolution of approximately 1 cm^{-1} using a grating of 1800 grooves/mm. For the temperature-dependent measurements, pressed pellets were placed separately in a Linkam cooling (THMS600) and heating (TS1500) stage for a range of 78 K to 920 K. Each spectrum was baseline corrected and fitted (Pseudo-Voigt) with the 'LAMP' software.²⁶

2.5 | Theoretical calculations

DFT calculations of the vibrational properties of $\text{Bi}_4\text{B}_2\text{O}_9$ were performed with the CASTEP code, which uses a combination of plane waves and pseudopotentials.²⁷ The calculations employed an energy cutoff of 900 eV and norm-conserving pseudopotentials from the Bennett-Rappe library.²⁸ Furthermore, the PBEsol exchange-correlation functional was used²⁹ and a $2 \times 2 \times 2$ Monkhorst-Pack grid of k -points was employed to sample the first Brillouin zone. To start with, the structure was optimized, relaxing all atomic coordinates, but fixing the unit cell parameters to the experimental values measured at 4 K. The subsequent calculations of the phonon density of states (PDOS), IR- and Raman-active modes made use of the variational density functional perturbation theory formalism.³⁰ These vibrational calculations used a $2 \times 3 \times 2$ Monkhorst-Pack grid of q -points. The total PDOS and the partial contribution of each atom in the asymmetric unit cell were plotted using a smearing of 0.1 THz (3.34 cm^{-1}).

The calculations of the Liebman density vector (LDV) were performed by means of the crystalline orbital program CRYSTAL14 employing the hybrid PW1PW method.^{31,32} Four different geometries were studied: the PW1PW-optimized structure (representing the 0 K data) and, the experimental structures at 293 K, 473 K, and 723 K; for which single-point calculations were used. LDV has been calculated for each of the four crystallographically independent bismuth atoms, using charge density distributions

calculated with a three-dimensional grid and a resolution of 5 pm created by the XCrySDen program.³³ The outputs of these calculations were processed with a Python script to calculate the LDV. In order to distinguish the LEP from the bonding- and oxygen-centered electrons, only the charge density within a 110 pm radius sphere centered on a given Bi-nucleus was plotted using the Wolfram Mathematica 8.0 program.³⁴

3 | RESULTS AND DISCUSSION

The starting parameters for the NPD data Rietveld refinements are taken from the single crystal data reported by Hyman and Perloff.¹⁸ The metric parameters of the monoclinic crystal structure ($P2_1/c$) at 4 K are given in Table 1.

At ambient conditions, both the metric parameters and the atomic coordinates are in excellent agreement with the reported ones.^{2,18} The NPD data Rietveld refinement plot of the low temperature (4 K) data are shown in Figure 3. About 3% weight fraction was identified as impurity of the cubic sillenite ($\text{Bi}_{24.5}\text{BO}_{38.25}$).⁷ Due to large number of atoms within a small fraction of the phase, Rietveld analysis does not converge for the refinement of the atomic coordinates of $\text{Bi}_{24.5}\text{BO}_{38.25}$ phase. However, the temperature-dependent evolution of the metric parameters of $\text{Bi}_{24.5}\text{BO}_{38.25}$ (Figure S1) could be followed along with model fit (see below). Temperature-dependent metric parameters of $\text{Bi}_4\text{B}_2\text{O}_9$ obtained from NPD (4 K-300 K) and XRPD (300 K-900 K) are shown in Figure 4. The thermal expansion coefficients

(TECs) calculated from the numerical differentiation for the crystal basis direction (\mathbf{a}_i) are also seen. Temperature dependency of TECs in the eigenvector directions along with four tensor component directions are given in Figure 5. Taking the whole temperature range into account the increase of the metric parameters (a , b , c and V) are nonlinear as well as the corresponding TECs (α_a , α_b , α_c , and α_V). The angle beta (β) decreases with increasing temperature. To better understand the thermal expansion of the monoclinic system, where the maximum and minimum expansion do not necessarily occur along the crystal basis directions, the bulk thermal expansion has been analyzed in terms of the associated tensor. This approach allowed to directly correlate the expansion property to the atomic arrangements of the system. The general form of the thermal expansion tensor is as follows:

$$\alpha_{ij} = \begin{bmatrix} \alpha_{11} & \alpha_{12} & \alpha_{13} \\ \alpha_{21} & \alpha_{22} & \alpha_{23} \\ \alpha_{31} & \alpha_{32} & \alpha_{33} \end{bmatrix} \quad (1)$$

which can be reduced to

$$\alpha_{ij} = \begin{bmatrix} \alpha_{11} & 0 & \alpha_{13} \\ 0 & \alpha_{22} & 0 \\ \alpha_{13} & 0 & \alpha_{33} \end{bmatrix} \quad (2)$$

for the monoclinic $\text{Bi}_4\text{B}_2\text{O}_9$ system. For a reference, we choose an orthogonal coordinate system $\{\mathbf{e}_1, \mathbf{e}_2, \mathbf{e}_3\}$ so that α_{ij} can be derived from the crystallographic basis vectors $\{\mathbf{a}_1, \mathbf{a}_2, \mathbf{a}_3\}$ according to the relations: \mathbf{e}_3 is parallel to \mathbf{a}_3 , \mathbf{e}_2 is parallel to \mathbf{a}_2^* (asterisk elsewhere refers to reciprocal space value) and $\mathbf{e}_1 = \mathbf{e}_2 \times \mathbf{e}_3$. The relationships³⁵ that

TABLE 1 Crystal structure of Bi_4BO_9 at 4 K obtained from neutron powder diffraction data Rietveld refinement

$a = 1108.655(16)$ pm, $b = 661.099(8)$ pm, $c = 1102.162(14)$ pm, $\beta = 91.1562(12)$, $R_{\text{wp}} = 0.0389$, $R_p = 0.0298$, $R_f = 0.0278$, GOF = 2.94.						
Atom	Site	Occupancy	x	y	z	$U_{\text{iso}}/\text{pm}^2 \cdot 10^4$
Bi1	4e	1.0	0.99278(21)	0.48249(35)	0.34757(21)	0.0084(5)
Bi2	4e	1.0	0.80501(20)	0.04773(32)	0.49120(22)	0.0077(5)
Bi3	4e	1.0	0.50205(21)	0.42353(35)	0.15855(24)	0.0103(4)
Bi4	4e	1.0	0.34172(22)	0.4372(4)	0.48105(22)	0.0091(5)
B1	4e	1.0	0.75226(29)	0.2329(5)	0.26495(29)	0.0119(7)
B2	4e	1.0	0.22466(25)	0.2561(5)	0.25474(29)	0.0114(6)
O1	4e	1.0	0.50007(35)	0.1043(6)	0.10644(35)	0.0142(8)
O2	4e	1.0	0.38323(32)	0.1002(5)	0.4968(4)	0.0109(7)
O3	4e	1.0	0.86350(35)	0.1536(6)	0.2828(4)	0.0136(8)
O4	4e	1.0	0.92154(32)	0.1541(5)	0.01280(34)	0.0133(8)
O5	4e	1.0	0.18757(32)	0.2130(5)	0.13954(34)	0.0120(9)
O6	4e	1.0	0.67674(29)	0.2294(6)	0.36705(32)	0.0113(8)
O7	4e	1.0	0.14618(32)	0.2477(5)	0.35219(30)	0.0093(7)
O8	4e	1.0	0.34190(31)	0.3236(5)	0.2801(4)	0.0142(8)
O9	4e	1.0	0.71251(32)	0.3155(6)	0.1567(4)	0.0138(8)

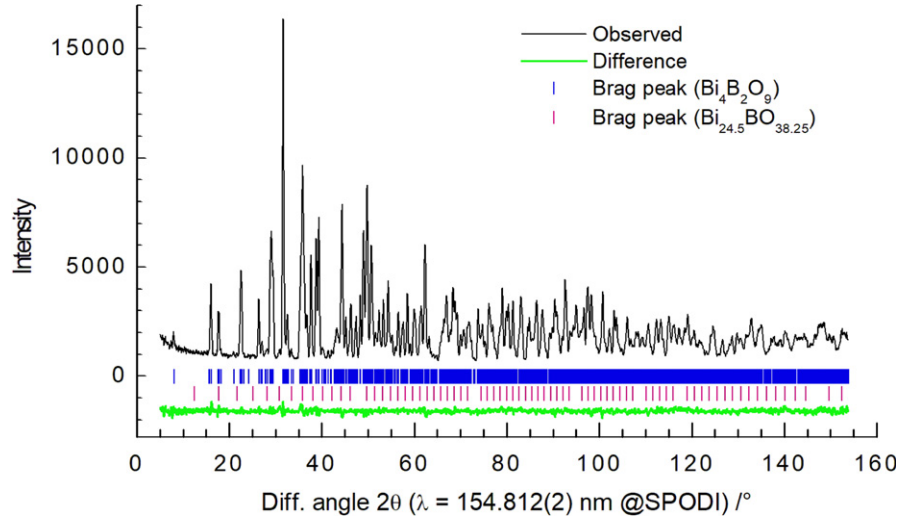


FIGURE 3 Neutron powder data (4 K) Rietveld plot. The second phase $\text{Bi}_{24.5}\text{BO}_{38.25}$ comprises of 3% phase fraction

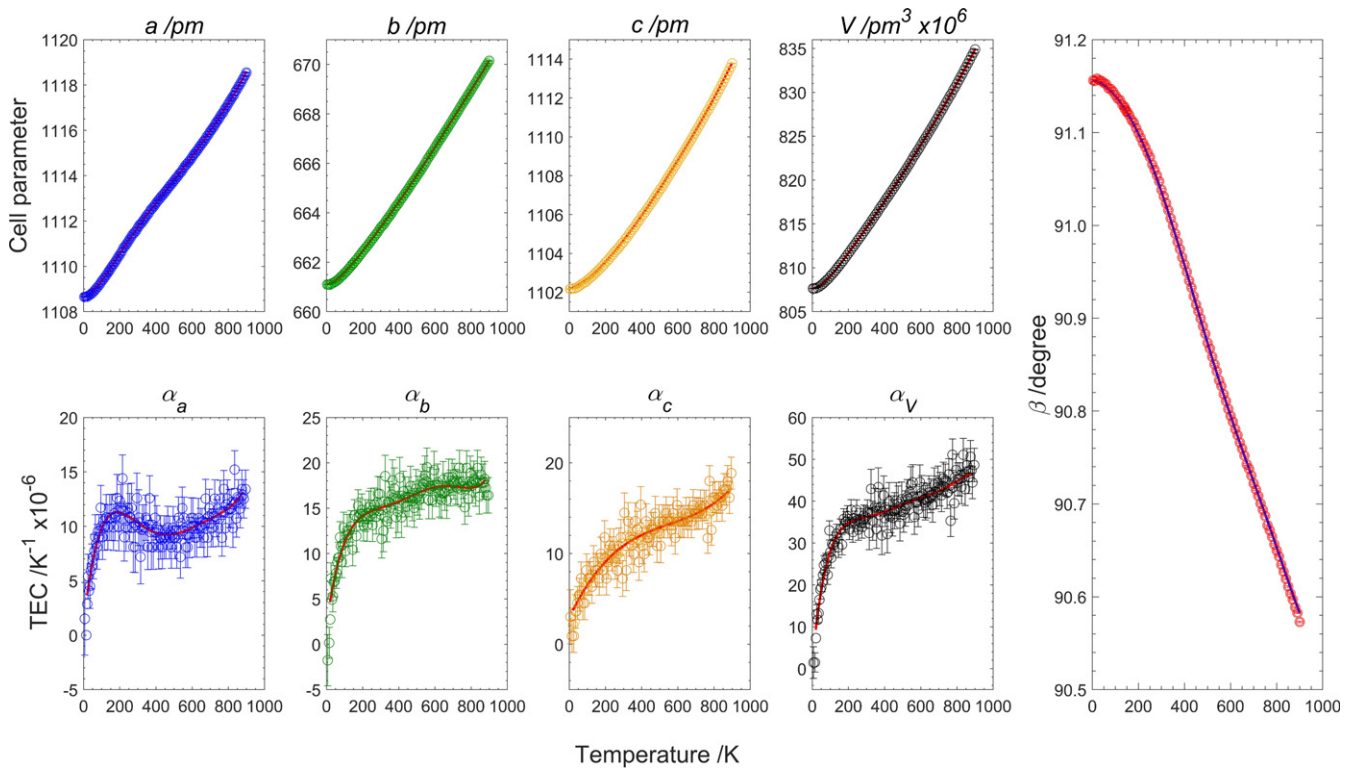


FIGURE 4 Temperature-dependent metric parameters and thermal expansion coefficients of $\text{Bi}_4\text{B}_2\text{O}_9$. The solid line represents the corresponding model fit

ensures the metric parameter c and b are parallel to \mathbf{e}_2 and \mathbf{e}_3 , respectively, can be expressed as follows:

$$\begin{pmatrix} \mathbf{a}_1 \\ \mathbf{a}_2 \\ \mathbf{a}_3 \end{pmatrix} = \begin{bmatrix} a \sin(\beta) & 0 & a \cos(\beta) \\ -b \sin(\alpha) \cos(\gamma^*) & b \sin(\alpha) \sin(\gamma^*) & b \cos(\alpha) \\ 0 & 0 & c \end{bmatrix} \cdot \begin{pmatrix} \mathbf{e}_1 \\ \mathbf{e}_2 \\ \mathbf{e}_3 \end{pmatrix} \quad (3)$$

Four independent tensor components of the TECs (α_{11} , α_{22} , α_{33} and α_{13}) are calculated. A representative TEC ellipsoid at 300 K is shown in Figure 5 along with cross-sections at some selected temperatures. In some recent

reports, we modeled the thermal expansion of some multi-type materials, using Grüneisen first-order and second-order approximations for the zero-pressure equation of states.^{36–41} For the present study we consider the first-order approximation where the temperature-dependent metric parameter (M) can be expressed as follows:

$$M(T) = M_0 + \frac{\gamma U(T)}{K_0} \quad (4)$$

M_0 refers to metric parameter at 0 K, possessing the zero-point energy. K_0 and γ are isothermal bulk modulus and thermodynamic Grüneisen parameter, respectively. K_0 was

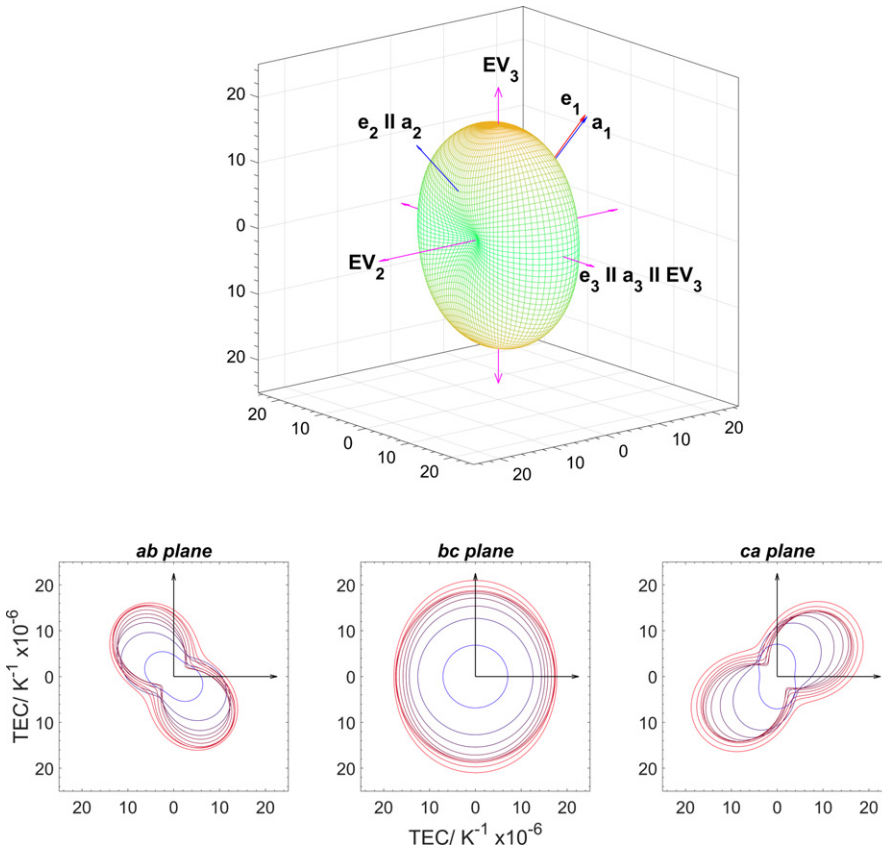


FIGURE 5 Top panel: Thermal expansion coefficient (TEC in 10^{-6}K^{-1}) ellipsoid of $\text{Bi}_4\text{B}_2\text{O}_9$ at 300 K. Here, \mathbf{e}_i , \mathbf{a}_i and \mathbf{EV}_i represent the Cartesian reference coordinate, crystal basis vector, and the Eigenvector, respectively. Bottom panel: The cross-sections of the TEC ellipsoids between 100 K and 900 K, where the distance from the origin to the edge of the representation surface indicates the change of the thermal expansivity in the given directions

calculated as 87.2(1) GPa from the measured 13 independent elastic coefficients²² using the Voigt-Reuss-Hill approximation⁴² which guarantees the estimate for a polycrystalline system. These elastic data estimate an average sound velocity of 1040(1) m/s and a Debye temperature of 130(1) K. It is well known that the calculation of vibrational energy $U(T)$ for polyatomic solids such as $\text{Bi}_4\text{B}_2\text{O}_9$ is difficult using a single Debye term in the quasi-harmonic approximation. That is, the parabolic Debye phonon spectrum with a characteristic cut-off frequency cannot truly represent the PDOS.⁴¹ Moreover, the calculated PDOS of $\text{Bi}_4\text{B}_2\text{O}_9$ shows two continua (see later), representing at least two Debye temperatures with/without additional Einstein terms depending on the temperature-dependent optical phonon dispersion. The α_V at high temperature clearly show that the TEC value departs from the Dulong-Petit saturation below 200 K. This is a clear hint of intrinsic anharmonicity the system possesses even at low temperature, which is not surprising for a system of four independent Bi^{3+} cations with stereochemically active LEPS. Thus, taking both isothermal and isochoric anharmonicity in the Grüneisen approximation the following expression properly describes the lattice thermal expansion of $\text{Bi}_4\text{B}_2\text{O}_9$:

$$M(T) = M_0 + \sum_{i=1}^D k_{Di} U_{Di}(T) + \sum_{j=1}^E k_{Ej} U_{Ej}(T) + \sum_{q=1}^A k_{Aq} U_{Aq}(T) \quad (5)$$

where M represents any of the metric parameters. The internal energy is contributed from Debye U_{Di} , Einstein

U_{Ej} long with the low-perturbed anharmonicity U_{Aq} terms.⁴³ The integral term of the Debye function is evaluated numerically. In our present approach, we take the Debye frequency in the anharmonicity term [3rd term in Equation (5)], thus represents the anharmonicity of the corresponding frequency. For a simplified case Equation (5) can be written as follows for the temperature-dependent metric parameters taking only the Debye terms:

$$a(T) = a_0 + \frac{\gamma_D}{K_0} U_{D1}(T) + \frac{\gamma_D}{K_0} U_{D2}(T) + \frac{1}{K_0} U_{AD}(T) \quad (5a)$$

$$b(T) = b_0 + \frac{\gamma_D}{K_0} U_D(T) + \frac{1}{K_0} U_{AD}(T) \quad (5b)$$

$$c(T) = c_0 + \frac{\gamma_D}{K_0} U_D(T) + \frac{1}{K_0} U_{AD}(T) \quad (5c)$$

$$V(T) = V_0 + \frac{\gamma_D}{K_0} U_D(T) + \frac{1}{K_0} U_{AD}(T), \quad (5d)$$

where γ_D refers to the isothermal Grüneisen parameter for the Debye term and U_{AD} represents the anharmonic contribution to the Debye spectrum. It is noteworthy to mention that the isothermal anharmonicity (Grüneisen parameter) was calculated for the Debye term whereas isochoric

TABLE 2 Fitting parameters of the thermal expansion of the metric parameters of $\text{Bi}_4\text{B}_2\text{O}_9$

Metric	M_0	θ_{D1}/K	θ_{D2}/K	$\hat{a}/10^{-5} \text{ K}^{-1}$	γ_D	K_0/GPa
a/pm	1108.65(1)	201 (20)	1250(77)	-87(5)	0.9(1)*	162(12)
b/pm	661.10(1)	200 (12)	-	-35(1)	0.9(1)*	241(2)
c/pm	1102.16(3)	217 (15)	-	-104(2)	0.9(1)*	248(3)
$V/\text{pm}^3 \cdot 10^6$	807.66(1)	157 (6)	-	-48(2)	0.9(1)*	87.2(1)

*Thermodynamic Grüneisen parameter (γ_D) was calculated taking the bulk modulus, which was fixed for the calculation of the axial bulk moduli; \hat{a} is the isochoric anharmonicity⁴⁴ and θ_{Di} to Debye temperature. $\beta(T) = 91.16 - 2.48 \times 10^{-5}T - 1.79 \times 10^{-6}T^2 + 5.18 \times 10^{-9}T^3 - 2.20 \times 10^{-11}T^4 + 4.76 \times 10^{-14}T^5 - 4.56 \times 10^{-17}T^6 + 1.60 \times 10^{-20}T^7$.

anharmonicity (\hat{a}) was calculated from the expression of the anharmonicity term, where the respective Grüneisen parameters were fixed to unity.³⁹ The excellent fit between the observed data and the model line for the metric parameters as well as for the TECs can be seen (Figure 4). The fitted parameters are given in Table 2.

The temperature-dependent isotropic displacement parameters (ADPs) obtained from the neutron data Rietveld refinements are shown in Figure S2 along with the fitting model based on the Debye approach suggested by Lonsdale.⁴⁴ The fitting parameters as given in Table S1 lead to a mass-weighted Debye temperature of 232(4) K. The zero-point motion (static disorder) and the vibrational amplitude of all the atoms are comparable irrespective to their significantly different masses, indicating the elastic nature of the system. Therefore, it would not be surprising that the acoustic phonon plays the dominating roles in determining the Debye temperature of $\text{Bi}_4\text{B}_2\text{O}_9$.

3.1 | Vibrational features

Factor group analysis predicts 180 modes ($45A_g + 45A_u + 45B_g + 45B_u$), where 90 modes are Raman active ($45A_g + 45B_g$), 87 are infrared active ($44A_u + 43B_u$) and modes $A_u + 2B_u$ represent the acoustic modes. The calculated phonon dispersion is shown Figure S3. The dispersion of three acoustic branches in two directions (Γ -Z and Γ -Y) estimate an averaged Debye temperature of (256(2) K). The total PDOS and the respective atomic contributions are plotted in Figure S4, showing that the low frequency region is exclusively contributed by the heavy atom bismuth. The contributions from the light atoms oxygen and boron spread over the whole PDOS. The PDOS can be described using two continua, where the low-frequency region (0 - 600 cm^{-1}) is compact and the high frequency region ($>600 \text{ cm}^{-1}$) is composed of some discrete optical modes. The sharp feature centered at about 890 cm^{-1} is a merged combination of two peaks centered at $889(1) \text{ cm}^{-1}$ and $891(1) \text{ cm}^{-1}$. The former one belongs to $\text{B}(2)\text{O}_3$ group (O(5), O(7) and O(8)) with an averaged $\text{B}(2)$ -O distance of 138.3 (5) pm, and the latter one to $\text{B}(1)\text{O}_3$ group (O(3), O(6) and

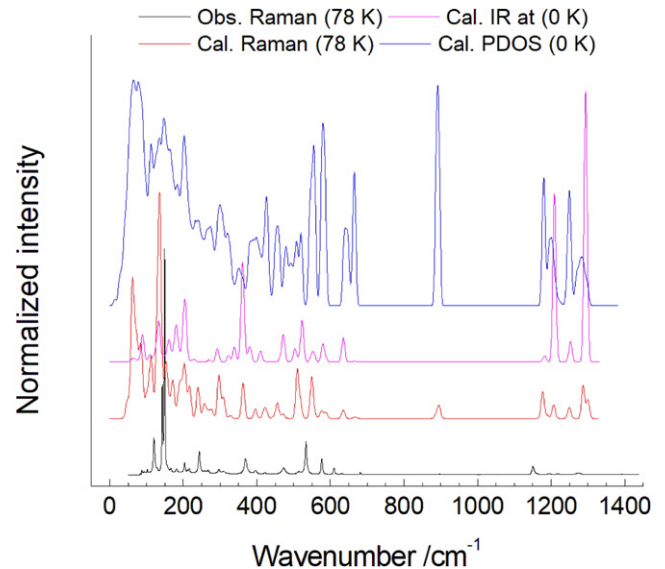


FIGURE 6 Comparative view between the phonon density of states (PDOS), Raman and infrared (IR) spectra of $\text{Bi}_4\text{B}_2\text{O}_9$

O(9)) with an averaged $\text{B}(1)$ -O distance of 137.8(5) pm. Spectral region above 1200 cm^{-1} is mainly due to rigid BO_3 groups, where a minor part is contributed by O(3), O(5), O(6), O(7), O(9) atoms. Here, O(1), O(2), and O(4) have almost no contribution to the high-frequency region as they are exclusively coordinated to bismuth atoms. Contributions of boron at the low frequency regions ($<400 \text{ cm}^{-1}$) can be explained due to Bi-O-B vibrations. Description of PDOS helps guide to understand how the microscopic features such as eigenvectors of any given atom contribute to the macroscopic heat capacity and thermal expansion of the bismuth-borate ceramics. Figure 6 shows a comparative view between the PDOS, the Raman and the infrared spectra, where the calculated Raman spectrum shows excellent agreement with that of the spectrum collected at 78 K. The temperature-dependent Raman spectra are shown in Figure S5 to understand the isochoric anharmonicity⁴⁰ which plays an important role at constant volume for a given system where LEPs are stereochemically active. Almost all the observed modes show usual

smooth softening with increasing temperature, which follows the Klemens decay.^{45,46} However, at least one mode associated with the BO_3 groups monotonically hardens till ~ 580 K followed by softening afterward as shown in Figure S6. The positive anharmonicity values of this mode indicates negative Grüneisen parameters, contributing to the contraction of any metric parameter with increasing temperature. The TEC anomaly in the **a**-direction can be correlated with the thermal behavior of this mode in the given temperature range (Figure 4).

3.2 | Lone electron pair

Although exploitation of LEPs has been an intense study of metal borates^{19,47,48} characterizations of LEPs using the Wang-Liebau eccentricity (WLE) parameter^{15–17} and the Liebau density vector (LDV)¹⁷ are recent but important developments. The WLE parameter has been calculated for each crystallographic independent bismuth atom (Bi(1), Bi(2), Bi(3), and Bi(4)) from the low-temperature neutron diffraction data of the crystal structures. In this case, the high-temperature crystal data were not included as the ADPs of the oxygen atoms obtained from the X-ray powder data cannot be refined with an accuracy comparable to those of neutron data. Since the WLE parameter is sensitive to the geometry of the BiO_x coordination, a constraint refinement between all oxygen atoms, using the X-ray data cannot adequately judge the temperature-dependency of the WLE parameter and was excluded. The temperature-dependent WLE of the Bi-coordination is shown in Figure 7. At about 20 K, each of the WLE parameters shows a steep decrease for all Bi atoms with increasing temperature, which remains almost constant up to 300 K for the Bi(1), Bi(2)-, and Bi(4)-coordination. The WLE parameter of the Bi(3) coordination experiences a steep increase at 120 K, which gradually decreases followed by a sudden drop at 310 K, and lies close to the averaged value. The temperature dependency of WLE of the Bi(3)-coordination ultimately shapes the averaged behavior which may be related to the change of the orientation of the eigenvector of the TECs (Figure 5) due to concomitant rigidity of the neighboring planar BO_3 group and high polarizability of the Bi(3) O_7 coordination. Considering the high-temperature WLE parameters,²² it can be concluded that the averaged stereochemical activity of bismuth atoms decreases with increasing temperature till decomposition/melting along with the minimum WLE value. Since the absolute value of WLE is a scalar, LDV can better describe the orientation of the LEP-lobe with respect to temperature. Herein, LDV describes the length of a vector directed from the nucleus of a Bi-atom to the maximum charge density of the LEP. LDV has been calculated for each Bi-atom for some selective temperatures using the charge density distributions of

the optimized structures as shown in Figure 8. The LDV points to the electron density associated with the stereochemical activity of the Bi^{3+} LEPs and their respective orientations with respect to the metric vector of the system. The sensitivity of orientation seems to be limited within the scope of the calculation, however, the LDV magnitudes clearly show their changes with increasing temperature as shown in Figure 9. The lowest averaged LDV value at 293 K is consistent with the lowest averaged WLE parameter. The sudden jump of the LDV at higher temperatures can be ascribed to the TEC anomaly in the **a**-direction.

4 | CONCLUSION

Debye temperature calculated from the elastic coefficients (130(1) K) lies close to the value calculated from the thermal expansion modeling (156(6) K). On the other hand, the averaged Debye temperature calculated from the phonon dispersions of three acoustic branches (252(2) K) is close to the value calculated from the isotropic atomic displacement parameters (232(4) K). However, they are significantly far away from the highest optical frequency observed by either Raman or PDOS at 1300 cm^{-1} (1871 K). The apparent inconsistency can be explained from the fundamental weighting factor associated with each approach.⁴¹ Since the vibration features of each atom are

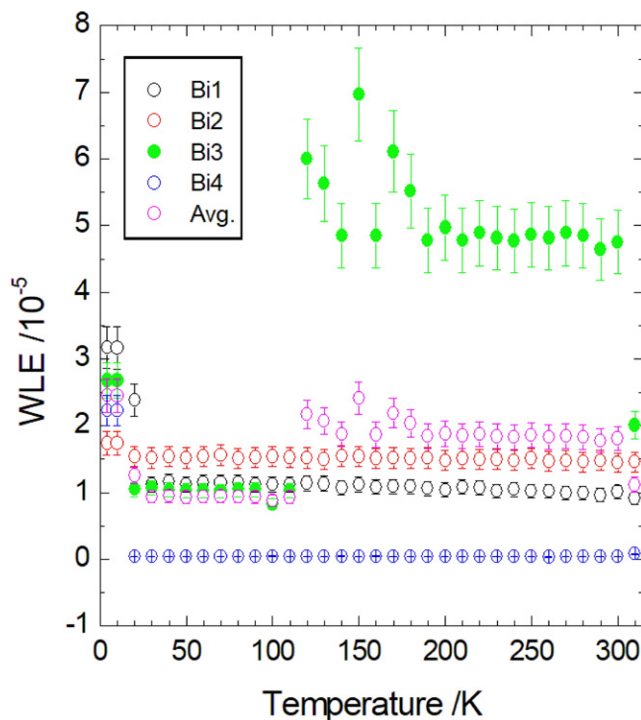


FIGURE 7 Temperature-dependent absolute value of the Wang-Liebau eccentricity (WLE) parameter of BiO_x coordination in $\text{Bi}_4\text{B}_2\text{O}_9$

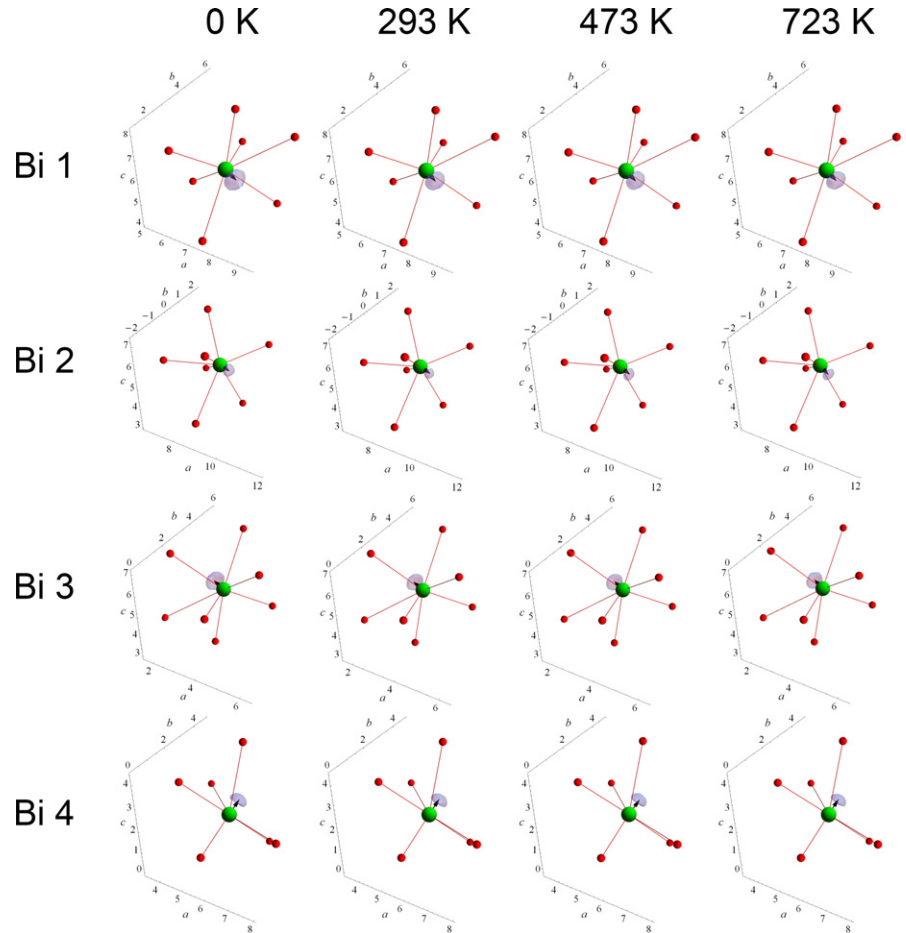


FIGURE 8 Temperature-dependent Liebau density vector (LDV) of $\text{Bi}_4\text{B}_2\text{O}_9$. Each arrow shows the magnitude and the orientation of LDV with the frame of the unit cell reference

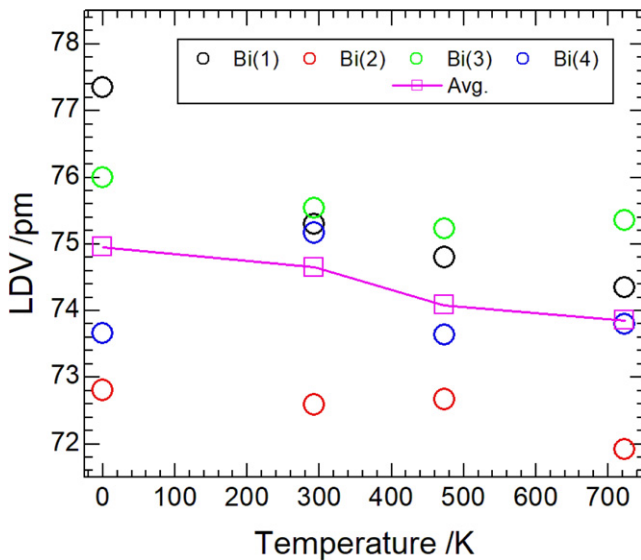


FIGURE 9 Temperature-dependent Liebau density vector (LDV) of Bi-atoms of $\text{Bi}_4\text{B}_2\text{O}_9$ compound obtained from the density functional theory calculations

comparable irrespective to the mass of the atoms, the Debye temperature seems to be dependent only on the low-frequency optic, or on the acoustic phonons. This

assumption can be further justified as there is no appreciable shift of the optical modes with respect to temperature. Considering the central frequency of the PDOS continua of bismuth at $\sim 110 \text{ cm}^{-1}$, the Debye temperature (158 K) matched to that of calculated from the DEA modeling. Unlike other bismuth borate ceramics, the $\text{Bi}_4\text{B}_2\text{O}_9$ crystal structure does not contain polymeric borate groups. Moreover, three oxygen atoms (O(1), O(2), and O(4)) are exclusively coordinated with the Bi-atoms. Therefore, the choice of the elastic Debye theory can better explain the vibrational dynamics of this bismuth borate. Both the Liebau eccentricity parameter and the Liebau density vector help understand how the orientation and the magnitude of the lone electron pair stereo-activity changes with respect to temperature. This study would particularly shed light on an in-depth microscopic understanding of relevant bismuth borate ceramics with Bi^{3+} cations.

ACKNOWLEDGEMENT

MMM gratefully acknowledges the University of Bremen for financial support. Neutron powder diffraction was performed at the SPODI instrument operated by JCMS at the MLZ, Garching, Germany, as the measurement facility was

sponsored by the scientific user division. MF is funded by the Central Research Development Fund (CRDF) of the University of Bremen (Funding line 04 - Independent Projects for Postdocs). CBM is member of the research staff of Consejo Nacional de Investigaciones Científicas y Técnicas (CONICET). MC is grateful to CONICET for his postdoctoral fellowship.

ORCID

M. Mangir Murshed  <http://orcid.org/0000-0002-9063-372X>

REFERENCES

- Hellwig H, Liebertz J, Bohatý L. Exceptional large nonlinear optical coefficients in the monoclinic bismuth borate BiB_3O_6 (BIBO). *Solid State Commun.* 1998;109(4):249–51.
- Muehlberg M, Burianek M, Edongue H, Poetsch C. $\text{Bi}_4\text{B}_2\text{O}_9$ -crystal growth and some new attractive properties. *J Cryst Growth.* 2002;239:740–4.
- Egorysheva AV, Burkov VI, Gorelik VS, Kargin YF, Koltashev VV, Plotnichenko VG. Raman scattering in monocystal $\text{Bi}_3\text{B}_5\text{O}_{12}$. *Phys Solid State.* 2001;43(9):1655–8.
- Blasse G, Oomen EWJL, Liebertz J. On the luminescence of the bismuth borates BiB_3O_6 and $\text{Bi}_3\text{B}_5\text{O}_{12}$. *Phys Stat Sol b.* 1986;137:K77–81.
- Levin EM, McDaniel CL. The system Bi_2O_3 – B_2O_3 . *J Am Ceram Soc.* 1962;45(8):355–60.
- Becker P, Froehlich R. Crystal growth and crystal structure of the metastable bismuth orthoborate BiBO_3 . *Z Naturforsch B.* 2004;59(3):256–8.
- Burianek M, Held P, Mühlberg M. Improved single crystal growth of the boron sillenite “ $\text{Bi}_{24}\text{B}_2\text{O}_{39}$ ” and investigation of the crystal structure. *Cryst Res Technol.* 2002;37(8):785–96.
- Kuzmicheva GM, Melnikova TI. Structural features of bismuth borates in the system $n\text{Bi}_2\text{O}_3$ – $m\text{B}_2\text{O}_3$. *Russ J Inorg Chem.* 2009;54(1):73–80.
- Teng B, Yu WT, Wang JY, Cheng XF, Dong SM, Liu YG. Bismuth octaborate, $\text{Bi}_2\text{B}_8\text{O}_{15}$. *Acta Crystallogr C.* 2002;58:25i–6i.
- Stein W-D, Cousson A, Becker P, Bohatý L, Braden M. Temperature-dependent X-ray and neutron diffraction study of BiB_3O_6 . *Z Kristallogr.* 2007;222:680–9.
- Vegas A, Cano FH, García-Blanco S. Crystal structure of $3\text{Bi}_2\text{O}_3$: $5\text{B}_2\text{O}_3$. A new type of polyborate anion $(\text{B}_5\text{O}_{11})^{7-}$. *J Solid State Chem.* 1976;17:151–5.
- Filatov SK, Shepelev YF, Aleksandrova YV, Bubnova RS. Structure of bismuth oxoborate $\text{Bi}_4\text{B}_2\text{O}_9$ at 20, 200, and 450°C. *Russ J Inorg Chem.* 2007;52(1):21–8.
- Burianek M, Muehlberg M. Crystal growth of boron sillenite $\text{Bi}_{24}\text{B}_2\text{O}_{39}$. *Cryst Res Technol.* 1997;32:1023–7.
- Jain A, Ong SP, Hautier G, Chen W, Richards WD, Dacek S, et al. Commentary: the materials project: a materials genome approach to accelerating materials innovation. *APL Mater.* 2013;1(1):011002.
- Wang X, Liebau F. Influence of lone-pair electrons of cations on bond-valence parameters. *Z Kristallogr.* 1996;211:437–9.
- Murshed MM, Fischer RX, Gesing TM. The role of the Pb^{2+} lone electron pair for bond valence sum analysis in mullite-type PbMBO_4 (M = Al, Mn and Fe) compounds. *Z Kristallogr.* 2012;227:580–4.
- Curti M, Gesing TM, Murshed MM, Bredow T, Mendive CB. Liebau density vector: a new approach to characterize lone electron pairs in mullite-type materials. *Z Kristallogr.* 2013;288:629–34.
- Hyman A, Perloff A. The crystal structure of bismuth (2:1) borate, $2\text{Bi}_2\text{O}_3$: B_2O_3 . *Acta Crystallogr B.* 1972;28(7):2007–11.
- Becker P, Bohatý L. Thermal expansion of bismuth triborate. *Cryst Res Technol.* 2001;36(11):1175–80.
- Filatov SK, Bubnova RS. Borate crystal chemistry. *Phys Chem Glass.* 2000;41(5):216–24.
- Sleight AW. Compounds that contract on heating. *Inorg Chem.* 1998;37(12):2854–60.
- Schreuer J, Mühlberg M, Burianek M, Wallrafen F. Influence of the Bi $6s^2$ lone electron pair on elastic properties of monoclinic $\text{Bi}_4\text{B}_2\text{O}_9$. *Z Kristallogr.* 2015;230(11):667–76.
- Hoelzel M, Senyshyn A, Juenke N, Boysen H, Schmah W, Fuess H. High-resolution neutron powder diffractometer SPODI at research reactor FRMII. *Nucl Instrum Methods Phys Res A.* 2012;667:32–7.
- Larson AC, Von Dreele RB. General structure analysis system (GSAS). *Structure.* 2004;748(LAUR 86-748):86–748.
- Toby BH. EXPGUI, a graphical user interface for GSAS. *J Appl Crystallogr.* 2001;34(2):210–3.
- Richard D, Ferrand M, Kearley GJ. Analysis and visualisation of neutron-scattering data. *J Neutron Res.* February 2013;1996(4):33–9.
- Clark SJ, Segall MD, Pickard CJ, Hasnip PJ, Probert MI, Refson K, et al. First principles methods using CASTEP. *Z Kristallogr.* 2005;220(5–6):567–70.
- Bennett JW. Discovery and design of functional materials: integration of database searching and first principles calculations. *Phys Procedia.* 2012;34:14–23.
- Perdew JP, Ruzsinszky A, Csonka GI, Vydrov OA, Scuseria GE, Constantin LA, et al. Restoring the density-gradient expansion for exchange in solids and surfaces. *Phys Rev Lett.* 2008;100(13):136406.
- Refson K, Tulip PR, Clark SJ. Variational density-functional perturbation theory for dielectrics and lattice dynamics. *Phys Rev B.* 2006;73(15):155114.
- Dovesi R, Orlando R, Erba A, Zicovich-Wilson CM, Civalleri B, Casassa S, et al. CRYSTAL14: a program for the ab initio investigation of crystalline solids. *Int J Quantum Chem.* 2014;114(19):1287–317.
- Bredow T, Gerson AR. Effect of exchange and correlation on bulk properties of MgO, NiO, and CoO. *Phys Rev B.* 2000;61(8):5194–201.
- Kokalj A. Computer graphics and graphical user interfaces as tools in simulations of matter at the atomic scale. *Comput Mater Sci.* 2003;28(2):155–68.
- Wolfram Research Inc. *Mathematica 8.0. Version 8.* Champaign, IL: Wolfram Research, Inc.; 2010.
- Pauffer P, Weber T. On the determination of linear expansion coefficients of triclinic crystals using X-ray diffraction. *Eur J Mineral.* 1999;11(4):721–30.
- Murshed MM, Gesing TM. Anisotropic thermal expansion and anharmonic phonon behavior of mullite-type $\text{Bi}_2\text{Ga}_4\text{O}_9$. *Mater Res Bull.* 2013;48(9):3284–91.

37. Murshed MM, Mendive CB, Curti M, Nénert G, Kalita PE, Lipinska K, et al. Anisotropic lattice thermal expansion of PbFeBO_4 : a study by X-ray and neutron diffraction, Raman spectroscopy and DFT calculations. *Mater Res Bull.* 2014;59:170–8.
38. Murshed MM, Mendive CB, Curti M, Šehović M, Friedrich A, Fischer M, et al. Thermal expansion of mullite-type $\text{Bi}_2\text{Al}_4\text{O}_9$: a study by X-ray diffraction, vibrational spectroscopy and density functional theory. *J Solid State Chem.* 2015;229:87–96.
39. Murshed MM, Zhao P, Fischer M, Huq A, Alekseev EV, Gesing TM. Thermal expansion modeling of framework-type Na $[\text{AsW}_2\text{O}_9]$ and K $[\text{AsW}_2\text{O}_9]$. *Mater Res Bull.* 2016;84:273–82.
40. Murshed MM, Šehović M, Fischer M, Senyshyn A, Schneider H, Gesing TM. Thermal behavior of mullite between 4 K and 1320 K. *J Am Ceram Soc.* 2017;100:5259–73.
41. Mangir Murshed M, Zhao P, Huq A, Gesing TM. Thermal expansion behaviors of $\text{Li}_3\text{AsW}_7\text{O}_{25}$: a case study for comparative Debye temperature for a large polyatomic unit Cell. *Z Anorg Allg Chem.* 2018;644(4):253–9.
42. Anderson OL. A simplified method for calculating the debye temperature from elastic constants. *J Phys Chem Solids.* 1963;24(7):909–17.
43. Oganov AR, Dorogokupets PI. Intrinsic anharmonicity in equations of state and thermodynamics of solids. *J Phys Condens Matter.* 2004;16(8):1351–60.
44. Lonsdale K. Vibration amplitudes of atoms in cubic crystals. *Acta Crystallogr.* 1948;1(3):142–9.
45. Klemens PG. Anharmonic decay of optical phonons. *Phys Rev B.* 1966;148(2):845–8.
46. Balkanski M, Wallis R, Haro E. Anharmonic effects in light scattering due to optical phonons in silicon. *Phys Rev B.* 1983;28:1928–34.
47. Dong X, Jing Q, Shi Y, Yang Z, Pan S, Poeppelmeier KR, et al. $\text{Pb}_2\text{Ba}_3(\text{BO}_3)_3\text{Cl}$: a material with large SHG enhancement activated by Pb-chelated BO_3 groups. *J Am Chem Soc.* 2015;137(29):9417–22.
48. Mutailipu M, Zhang M, Zhang B, Yang Z, Pan S. The first lead fluorooxoborate $\text{PbB}_5\text{O}_8\text{F}$: achieving the coexistence of large birefringence and deep-ultraviolet cut-off edge. *Chem Commun.* 2018;54(49):6308–11.

SUPPORTING INFORMATION

Additional supporting information may be found online in the Supporting Information section at the end of the article.

How to cite this article: Murshed MM, Petersen H, Fischer M, et al. Thermal properties of 2:1 bismuth borate: Temperature-dependent characterizations of lone electron pairs. *J Am Ceram Soc.* 2018;00:1–11. <https://doi.org/10.1111/jace.16042>